FISFVIFR

Contents lists available at ScienceDirect

International Journal of Plasticity

journal homepage: www.elsevier.com/locate/ijplas





Influence of cementation on the yield surface of rocks numerically determined from digital microstructures

Martin Lesueur a,b,c,*, Manolis Veveakis a, Hadrien Rattez d

- ^a Civil and Environmental Engineering, Duke University, Durham, NC 27708-0287, USA
- ^b School of Earth Sciences, University of Western Australia, Crawley, WA 6009, Australia
- ^c Faculty of Civil Engineering and Geosciences, Delft University of Technology, Delft, 2628CN, Netherlands
- d Institute of Mechanics, Materials and Civil Engineering (IMMC), Université Catholique de Louvain, Louvain-la-Neuve, B-1348, Belgium

ARTICLE INFO

Keywords: Yield surface Cementation Upscaling Finite Element Method µCT-scan

ABSTRACT

Digital Rock Physics has reached a level of maturity on the characterisation of primary properties that depend on the microstructure - such as porosity, permeability or elastic moduli - by numerically solving field equations on μCT scan images of rock. After small deformations or at depth though, most rocks eventually reach their limit of elasticity and the complementary plastic properties are needed to describe the full mechanical behaviour. Currently, determination of a rock's yield surface from its microstructure is often restricted to semi-analytical criteria derived by limit analysis or numerical simulations performed on idealised geometries. Such simplification lacks representativeness, particularly for processes that affect directly the pore-grain interface such as the cementation phenomenon, happening during diagenesis. Eventually, only direct numerical simulation of elasto-plasticity performed on digitalised microstructures can be used to assess the strength of different cemented materials and its evolution with the alteration of the microstructure. In this study, we provide a comprehensive parametric study on the impact of cementation on rock strength for real microstructures of cemented granular materials. Compared to most previous studies, the whole yield surface is determined numerically (using Finite Element Method) in order to assess the influence of cementation for different stress-paths. The previously known tendency of rock to strengthen with increasing cementation volume is verified. New results on the influence of cement property namely Young's modulus, friction and cohesion on the rock's yield surface are explored. The envelopes obtained are compared to the ones obtained by experimental data and existing models. The framework presented in this study showcases the wider possibility of determining any rock's or porous material's yield surface from its microstructure.

1. Introduction

The characterisation of rock properties has been revolutionised by the emergence of the discipline of Digital Rock Physics (DRP). The concept of such workflow is to infer various rock properties from numerical simulations performed on real microstructures obtained from μ CT scans of the rock considered (Andrä et al., 2013; Dvorkin et al., 2011). It relies on the fact that past a given sample size, named Representative Elementary Volume (REV), which depends both on the microstructure and the property studied, the property homogenised on this small sample is representative of the rock at the larger scale of interest (Hill, 1963). This approach relies on non-destructive testing which can become a considerable advantage when the rock sample is difficult to obtain in large

https://doi.org/10.1016/j.ijplas.2022.103338

Received 12 January 2022; Received in revised form 4 May 2022

Available online 27 May 2022

0749-6419/© 2022 The Author(s). Published by Elsevier Ltd. This is an open access article under the CC BY license (http://creativecommons.org/licenses/by/4.0/).

^{*} Corresponding author at: School of Earth Sciences, University of Western Australia, Crawley, WA 6009, Australia. E-mail address: m.lesueur@tudelft.nl (M. Lesueur).

quantities (Arns et al., 2004). Additionally, different types of tests can be performed on the same sample which prevents errors linked to the spatial variability of heterogeneous rocks (Andrä et al., 2013). Lastly, the flexibility of numerical methods allows to set up more complex analysis than experiments (Dvorkin et al., 2008).

With the everlasting development of numerics, DRP is reaching new heights. After the large improvement of μ CT scan images characterisation (Cnudde and Boone, 2013; Sarker and Siddiqui, 2009), permeability computation on μ CT scan images is also attaining its scientific maturity (Blunt et al., 2013; Saxena et al., 2018). In turn, this leaves place to the discovery of new properties that could be obtained with DRP. We are interested in this contribution in the upscaling of mechanical properties of rocks. While the upscaling of the elastic moduli is already heavily studied (Arns et al., 2002; Saxena and Mavko, 2016; Liang et al., 2020), contributions relating to the upscaling of plastic properties remains scarce, despite the rising importance for the characterisation of a rock's plasticity, in parallel with the development of unconventional resources exploitation, or the underground storage of nuclear waste and CO_2 (Hueckel and Pellegrini, 2002). In those environments where the risk of triggering plastic deformations of the rock is higher than usual due to the conditions of pressure and temperature at depth, safe operations can only be ensured with the knowledge of rock strength and its evolution with the alteration of the microstructure.

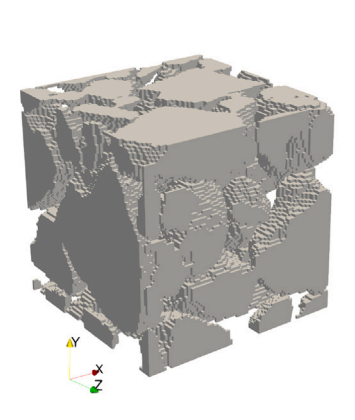
For that reason, the role of the structure of the rock needs to be directly accounted for, when simulating plasticity. Indeed, the granular origin of most rocks entails interaction forces between those grains. Those contact forces are commonly modelled with the Discrete Element Method (DEM) (Cundall and Strack, 1979). While the advantage of this technique lies undeniably in its scalability, the approximation of the grains as idealised spheres remains its strong limitation. Still, Level-Set Method (coupled with DEM) was used to compensate this weakness (Kawamoto et al., 2018). The other possibility is to rely on the Finite Element Method (FEM), that allows to take into account the exact microstructure from μ CT scan images. The algorithms have been already introduced and used in Lesueur et al. (2017, 2020b). FEM allows additionally for a simple coupling of the mechanics with different physics such as chemical reactions (Lesueur et al., 2020a; Guével et al., 2020) necessary for the cementation in this contribution. In light of the complexity elaborated in this paragraph, Lesueur et al. (2021) showed that simulations of plastic deformations could be lighter in terms of knowledge and computational resources if the upscaling of the material's plastic properties was narrowed down to the yield strength. We follow this direction in this contribution.

In a more general context, the yielding of porous materials has already earned a lot of interest in other fields of materials science. Yield criteria have been developed on idealised models of porous materials, starting with the hollow sphere model (Gurson, 1977), that consists of one single spherical pore. The advantage of using those simple models, is that semi-analytical solutions can be derived (Chen, 1975). While Gurson was the first one to propose such yield criterion, his model was greatly improved afterwards (Needleman and Tvergaard, 1987) and is still extended to various configurations (Besson, 2009). Examples of notable improvements are the consideration of more complex pore shape (Gologanu et al., 1993; Madou and Leblond, 2012), interactions between pores or dual porosity matrix (Vincent et al., 2014; Shen and Shao, 2016), void size effect (Wen et al., 2005), or the effects of hydrostatic stress and the third invariant of stress deviator (Gao et al., 2011). This discipline was developed originally for metal sheets, dealing with void nucleation and growth (Needleman and Tvergaard, 1987) and is still widely used nowadays (Reddi et al., 2019; Leclerc et al., 2020; Meade et al., 2021). Inversely, the difference gap between the idealised models of pore structure (Fritzen et al., 2012) and the heterogeneous nature of real rock microstructure prevents these theories to be applied as often on rocks. Yet, two specific features are making this research become more and more valuable for rock mechanics. The first one is the consideration of the pressure sensitivity of the matrix in the yield criterion (Shen et al., 2017, 2020). Indeed, most geomaterials are highly pressuresensitive (Jaeger, 2007) and this particularity influences greatly the shape of the yield surface (Drucker and Prager, 1952). The second is the derivation of the full surface of the yield envelope, from the tensile cut-off to pure shear and finally to the compaction cap. Studies on the evolution of rock strength was for a long time restricted to the sole consideration of the Uniaxial Compressive Strength as it is easier to assess experimentally (Bienawski, 1974). However, with unconventional resources being found deeper and deeper, subsurface operations can now reach the cap of the rock's yield surface in compaction. In that case, an extension to the characterisation of the entire yield envelope instead becomes necessary.

By using DRP, this contribution fills the gap from previous yield criteria of accounting for the exact microstructure of rocks. To the authors' knowledge, while most contributions still focus on extending Gurson-type criteria to more complex but still idealised microstructure (for example Cao et al., 2018), only Liu et al. (2017) simulated the real microstructure, yet they only looked at the homogenisation of frictional properties. Our suggested framework allows to compute the whole yield surface of a given digital rock sample, which will help further understand the influence of the rock microstructure on its yield surface. In order to go one step further and make use of the full capabilities of the framework presented, we extend the classically static studies to dynamic and characterise the evolution of the yield surface due to the alteration of the microstructure. The alteration process we are interested in is one that is known to influence greatly rock strength, a rock's cementation.

Cemented granular materials is a general class of geomaterials composed of grains connected by cement partially or completely filling the void in-between the grains. After deposition and consolidation phases of the sediments, cementation happens during diagenesis when mineral matter precipitates at the pore-grain interface (Worden and Burley, 2009). This process is known to increase the strength of the geomaterial by creating a cohesion between the particles (Bernabé et al., 1992; Yin and Dvorkin, 1994; den Brok et al., 1997). As such, it is critical to characterise for material stability applications in geotechnical engineering and geophysical processes. Unfortunately the phenomenon is complicated to reproduce at laboratory scale (Huang and Airey, 1998), because it takes place at a geological timescale. Instead research focuses on the production of artificially cemented materials that can achieve levels of strength similar to naturally cemented materials (Bernabé et al., 1992; Yin and Dvorkin, 1994; Delenne et al., 2009).

Several constitutive models have been developed to describe the behaviour of cemented granular materials at the continuum level based on elasto-plasticity (Gens and Nova, 1993; Nova et al., 2003; Rattez et al., 2018), but the link between the internal



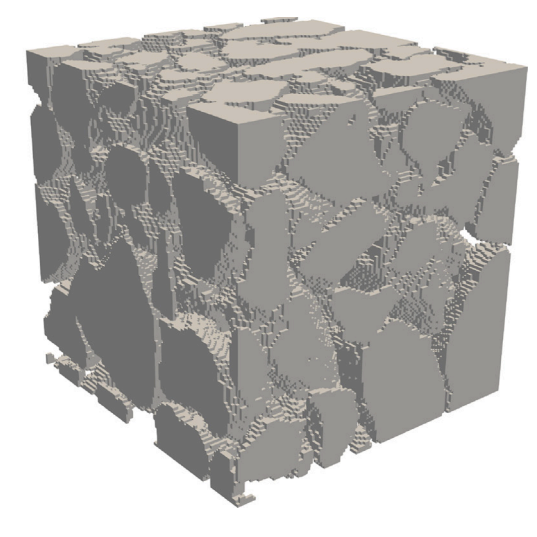


Fig. 1. Two cubic samples of the LV60 A sandpack, of respective size 0.8 mm (80 pixels) and 1.2 mm (120 pixels).

variables and the microstructural processes was not clear. To this end, Tengattini et al. (2014) have proposed a model describing the mechanical behaviour of cemented geomaterials relating grain breakage and cement damage at the microstructure to the evolution of inelastic strain, but the microstructure geometry was only described in this model by the porosity, a grading index and grain/cement volume fractions. Prioritising on the general applicability of the model, accuracy may still be lost on a case by case basis because cementation depends heavily on the rock microstructure (Leroueil and Vaughan, 1990) and the initial distribution of chain forces. Eventually, only direct numerical simulation of elasto-plasticity performed at the micro-scale level and coupled with microstructure evolution can be used to determine the strength of the cemented material. A few studies have already started the investigation using DEM with idealised microstructures (Gao and Kang, 2017; Estrada and Taboada, 2013), and provide valuable insight into the behaviour of cemented geomaterials at the microstructural level, but they cannot to capture the full complexity of these materials due to a lack of proper description of the microscale failure mechanisms and representative microstructal geometry.

We suggest using micro-scale mechanical simulations to reproduce the cementation happening during burial of rocks and predict the change of mechanical properties of the system. Particularly in this contribution, we are interested in the influence of the cementation on the yield surface of the material and how the mechanical properties of the cement affect it.

2. Numerical homogenisation of yield surface from digital rock

2.1. Finite element framework for digital rock mechanics

In this section we present the Finite Element framework used to simulate a mechanical loading on a digital rock.

Digital rock samples are reconstructed from a stack of 2D segmented μ CT scans, following the methodology presented in Lesueur et al. (2017). For geometry consistency, each voxel of the 3D μ CT scan corresponds to an element of the mesh. The result is a structured mesh of the cubic sample of rock microstructure. Compared to Lesueur et al. (2017) that studied hydromechanical couplings, we do not need the pore space in this contribution and it is therefore removed from the mesh to improve memory consumption. In this contribution, we exclusively use the LV60 A sandpack (Imperial College Consortium On Pore-Scale Modelling, 2014), whose microstructure is shown in Fig. 1 for different sample sizes. The mean grain diameter of this sand is 250 μ m, which corresponds to a sandstone of medium grain size following the Udden Wentworth grain-size scale, when those grains are cemented.

Mechanical loading is simulated in Finite Element by solving the momentum balance of a boundary value problem. We solve, on the grains, the divergence of stress,

$$\nabla \tilde{\sigma} = 0.$$
 (1)

On the outer faces of the sample, transient Dirichlet boundary conditions of displacement are imposed, to reproduce velocity-controlled loading. Note that the grains are assumed in this modelling not to undergo relative displacement at the intergranular contacts because we are interested in cemented rock. The cementation (implemented in the following section) prevents any possible movement. Linear elasticity is assumed, defined by a Young's modulus and a Poisson's ratio. For the selection of the plastic model, we first note that in our configuration, the stress is exclusively located at the grain contacts as can be seen in Fig. 2. Indeed, grain contacts are the weakest point in a granular structure, which is the reason why they enter plasticity first. For simulating plasticity at the grain contacts, two models are commonly used: J2 and Drucker–Prager. The J2 criterion is expressed as

$$\tilde{q}_{y} = C_{g},\tag{2}$$

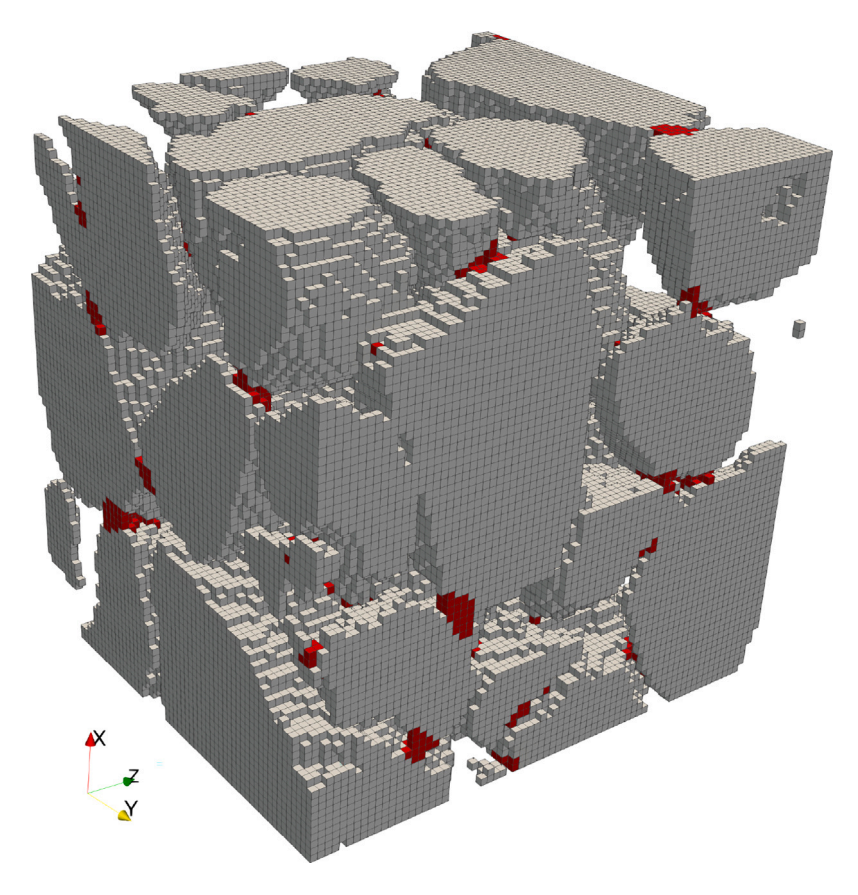


Fig. 2. Highlight (in red) of elements in plasticity at yielding state. Plasticity is assessed by finding elements for which $\tilde{q} = \tilde{q}_y$. Corners were cropped to remove boundary effects for clear visualisation. (For interpretation of the references to colour in this figure legend, the reader is referred to the web version of this article.)

with \tilde{q}_y the Von Mises stress at yield and C_g the cohesion of the grains. The material is assumed pressure-independent and can only fail in shear. This behaviour is representative of unconsolidated media. The Drucker Prager criterion is expressed as

$$\tilde{q}_{y} = C_{g} + tan(\phi_{g})\tilde{p}_{y},\tag{3}$$

with \tilde{p}_y the mean stress at yield and ϕ the friction angle. This is a continuum model of frictional contacts. In this contribution focused on cementation, we assume J2 plasticity for the grains as they are commonly stronger than the cement and will therefore experience only limited plastic deformation.

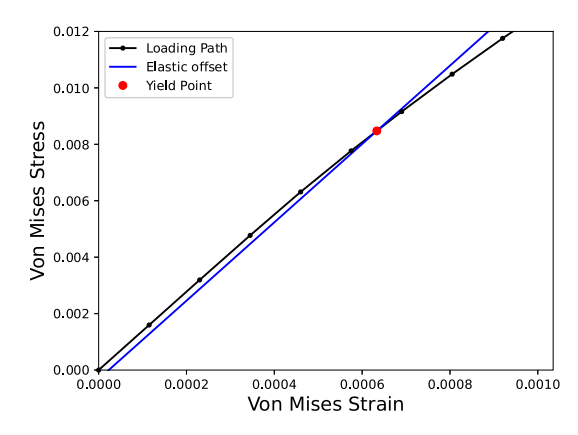
2.2. Numerical homogenisation scheme

Values of stress in laboratory experiments are measured as best as it possibly can be. Because stress is a virtual concept, its measurement can only be made through the displacement of a loading cell of which the relationship between stress and strain is known. For this reason, only an averaged value of the stress on the top face of the sample, (on which the loading cell is applied) can be measured. This is however a poor representation of the total stress experience by the full sample. With direct numerical simulations instead, the values of stress are known for each element constituting the mesh and the stress can this time be averaged on the whole sample. Through a rigorous homogenisation scheme, representative values can therefore be obtained. Specifically, the simulation needs to respect the Hill–Mandel condition (Hill, 1963) which postulates that the integral of the local mechanical work should be equal to the global mechanical work of the full sample.

$$\langle \tilde{\sigma}_{ij} \rangle_{\Omega} \langle \tilde{\epsilon}_{ij} \rangle_{\Omega} = \langle \tilde{\sigma}_{ij} \tilde{\epsilon}_{ij} \rangle_{\Omega}$$
 (4)

with $\langle \cdot \rangle_{\Omega} = \frac{1}{|\Omega|} \int_{\Omega} \cdot dV$, Ω being the grains. In short, this lemma describes a conservation of energy across the scales. The two paragraphs below describe the set-up of our specific problem for this Hill–Mandel condition to be respected in terms of strain and stress.

Regarding the strain, we first note that the loading condition is actually specific to the homogenisation theory itself, as the sample has to be subjected to an homogeneous macroscopic rate of deformation D_{ij} . Consequently, we impose the velocity $\tilde{v}_i = D_{ij}x_j \ \forall x \in \partial \Omega$, the external surface. As a result, we can write the homogenised strain for the structure as $\varepsilon_{ij} = D_{ij}t$.



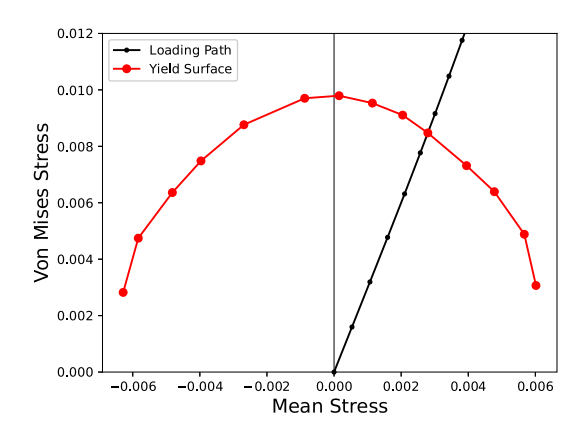


Fig. 3. Yield surface determination: (a) Offset method on the stress-strain curve of one loading; (b) Reported yield stress point on the yield surface, in comparison to its stress-path.

The corresponding macroscopic stress is defined as the average of the stress over the total volume Ω_{tot} . Since the material is considered dry, the pore space is not pressurised. This translates to a traction-free boundary at the inner surface which is directly imposed through the natural boundary conditions emerging in the weak form when using the divergence theorem on the divergence of stress. Eventually the macroscopic stress can be expressed in terms of the porosity as

$$\sigma_{ij} = \langle \tilde{\sigma}_{ij} \rangle_{\Omega_{tot}} = (1 - n)\langle \tilde{\sigma}_{ij} \rangle_{\Omega} \tag{5}$$

with n the porosity. In order to visualise the yield surface of the material, we are particularly interested in the mean stress $p = \sigma_{ii}$ and the Von Mises stress of the material, defined as $q = \sqrt{\frac{3}{2} s_{ij} s_{ij}}$ with s_{ij} being the deviatoric stress tensor. Note that all values of stress in this contribution are normalised with the Young modulus of the granular phase.

It was verified by Lesueur et al. (2020b) that these definitions along with proper boundary conditions resulted in the equivalence of local and global work defined in Eq. (4).

2.3. Yield surface measurement

In this contribution, we follow the typical procedure to determine the yield surface of the material. Multiple loadings of different stress paths are simulated until they reach the yield stress, measured with the offset method on the stress–strain curve as an arbitrary deviation of linear elasticity. This marks one point on the yield surface on the material. The full surface can then be interpolated from all the different points gathered. We note that this numerical determination of the yield presents a large advantage compared to the alternative experimental method. The yield surface of one specific sample can be easily obtained. Instead for the destructive experimental method, multiple different samples have to be destroyed in order to obtain one yield surface and leads to errors due to the spatial variability of microstructure within a rock. The use of kinematic boundary conditions provides us with an upper bound value of the yield stress, obtained from the state of maximum entropy production (Veveakis and Regenauer-Lieb, 2015). We note that a more quantitative study should also perform the study with stress-imposed boundary conditions to obtain the corresponding lower bound value.

In order to map the yield surface in the p-q space, we need to impose different stress paths while still respecting a homogeneous macroscopic rate of deformation to comply with the Hill–Mandel condition. A conventional triaxial loading does not respect this condition. We choose to follow the loading function used by Fritzen et al. (2012) analysis and have the velocity imposed on the sphere expressed as:

$$v_x = \dot{\epsilon}_0(\alpha + \beta)x,\tag{6}$$

$$v_{y} = \dot{\varepsilon}_{0}(-\alpha + \beta)y,\tag{7}$$

$$v_z = \dot{\epsilon}_0 \beta z$$
 (8)

with $\dot{\epsilon}_0$ the reference loading strain rate and α and β parameters controlling the triaxiality of the stress path, governed by the ratio $\frac{\alpha}{\epsilon}$.

Positive values of $\dot{\epsilon}_0$ corresponds to an extension of the sample while negative values correspond to its compression. This type of boundary condition allows to simulate both extension and compression in the same manner. This is an impossible task experimentally and most yield surfaces of rock are therefore only measured in compression which is the simpler process. This methodology presents therefore a great opportunity to explore all the different regimes of rock deformation. Note that the loading described by Eq. (8) has a principal axis of loading in x. By setting $\dot{\epsilon}_0$ negative, the principal axis of loading becomes y. To prevent this, v_x and v_y are switched when changing the sign of $\dot{\epsilon}_0$. Otherwise the anisotropy of the sample would prevent the positive and negative parts of the yield surface to connect. This anisotropy is showcased in Fig. 4. We can observe a slight difference of the yield surface shape

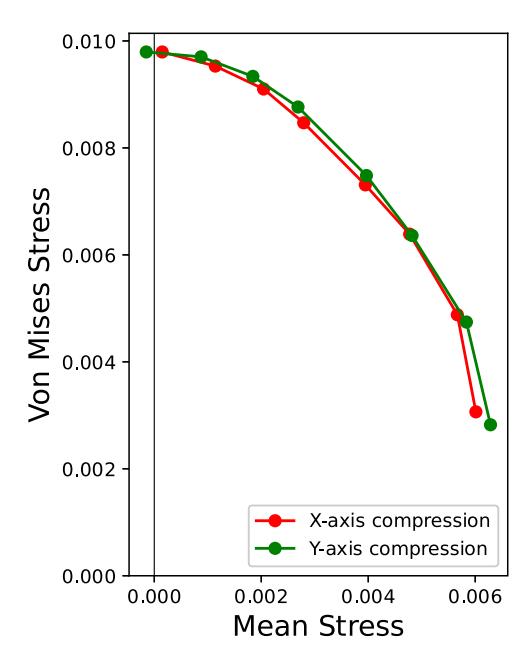


Fig. 4. Comparison of yield surfaces computed either with a compression in the X-axis (as followed in this contribution) or Y-axis.

Table 1 Example of different combinations of α and β values that correspond to loading paths of different triaxiality ratios following Eq. (8). The loadings vary from pure shear on the left to almost isotropic on the right.

Alpha	1	1	1	1	1	0.9	0.5	0.2
Beta	0.0	0.1	0.3	0.5	0.7	1	1	1

(almost negligible because sandpack is known to be isotropic) and the non-alignment of the point indicates that the homogenised elastic modulus is also different. The insignificance of the difference could be inferred from the known isotropy of a sandpack.

The different combinations of α and β used to map the yield surface, from pure shear to isotropic compression or extension can be found in Table 1. Note that isotropic extension or compression do no seem to produce sensical results in this contribution and are therefore not presented. Since (Lesueur, 2020) managed to get good results for the isotropic compression using the same methodology on the hollow sphere but with a conforming mesh, we can only infer that the problem comes from our non-optimised structured mesh.

Examples of the yield surfaces obtained with this methodology can be seen in Fig. 5, which shows the differences obtained by selecting a different grain model as discussed in the previous subsection.

2.4. REV size

Homogenised results at the micro-scale can be representative of global rock properties if the homogenisation is carried out at a sample size bigger than the REV size. Indeed, rock properties converges to a unique value past a certain sample size considered for the homogenisation. This size corresponds to containing a large enough number of grains that can represent the global granular behaviour of a even larger sample.

The REV size should be assessed in regards to the property studied. It has been shown for example that the convergence of the porosity does not necessarily suffice to reach the REV size of other properties (i.e. permeability Mostaghimi et al., 2012). In our case, we assess the convergence of the desired yield surface, for the LV60 A sandpack. Cubic samples of size 0.8 to 1.2 mm are tested, which are meshed at image resolution with 80 to 120 elements per length. Both end members are shown in Fig. 1. Note that all samples are selected from the same position in the μ CT scan. For each sample size, the yield surface is computed and plotted in Fig. 6a. We can observe that the yield surface monotonously shrinks with increasing sample size. To quantitatively assess convergence, we look at the evolution of the error to the final yield surface computed. The results are obtained first for the macro-cohesion, interpolated to p=0 and plotted in Fig. 6b. Then, to obtain an overall convergence of the whole yield surface, we compute the error made per triaxial ratio, i.e. for every loading path considered, with regards to the distance from the origin. We then plot in Fig. 6c the error averaged over the whole yield surface and the error bounds. We can observe that the error from both figures is steadily decreasing with a convergence trend indicating that the REV size would be soon reached, that we estimate around a length of 150 voxels.

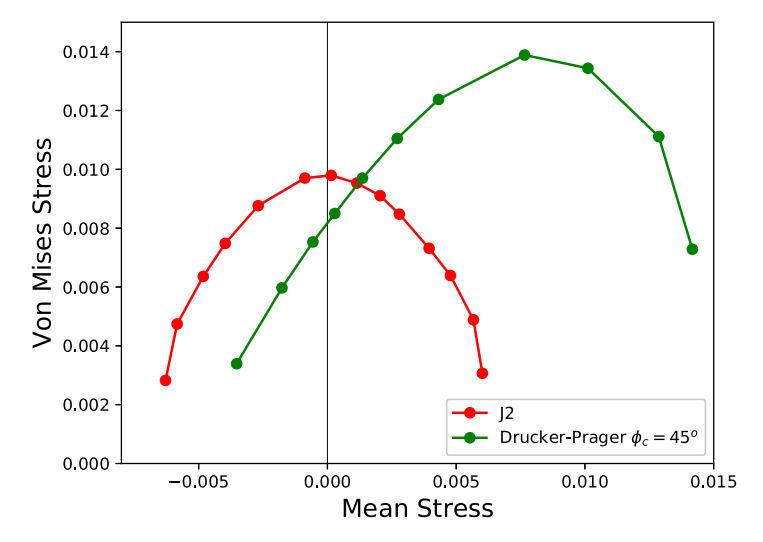


Fig. 5. Comparison of yield surfaces obtained with either a yield criterion J2 or Drucker-Prager for the granular skeleton.

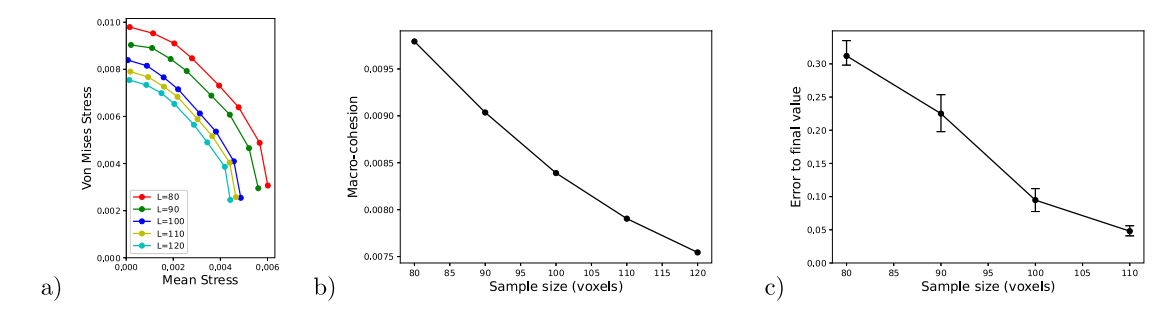


Fig. 6. Assessment of REV convergence.

As mentioned earlier, we note that for all samples, the REV size of porosity has already been reached, equal to \approx 38.6% as confirmed by Mostaghimi et al. (2012). Additionally, the REV size of permeability is reached at \approx 100 voxels (Mostaghimi et al., 2012; Lesueur et al., 2017). The new result that the REV size of the yield surface corresponds to an even larger size emphasises the interesting notion that REV convergence should be assessed for the specific property measured.

For computational purposes, we select the cubic sample of 80 voxels length for all the simulations in this contribution. We verified in this section that the sample selected retains the shape of the final yield surface at REV size without significant variations. In that sense, the sample still qualifies as Statistical REV (Zhang et al., 2000), defined as the size after which variations remain bounded and decrease monotonously with increasing size. Not selecting a sample past the REV size prevents us from providing quantitative results. However, this contribution is a qualitative study about the influence of certain parameters on the yield surface. For that purpose, the trends shown in this paper remain correct.

3. Parametric study of cementation on rock yield surfaces

This section focuses on the study of the influence of cementation on rock yield surfaces. Having introduced in the previous section the framework to upscale yield surfaces from rock microstructure, we now present the algorithm used to simulate the cementation process. Then, parametric studies are conducted.

3.1. Digital rock cementation algorithm

Cementation is known to be stress-dependent and preferably occurs at the grain contacts. However, uniform cement growth is commonly assumed instead, as a first approximation (Mousavi and Bryant, 2013). The simulation of this process is done with the erosion algorithm from Lesueur et al. (2020b). This algorithm was used to simulate uniform dissolution/precipitation and simplifies the problem to changing the domain of the layer of elements at the pore-grain boundary from pore to grain or vice versa. Different levels or volumes of cementation can be obtained by running the algorithm a multiple number of times. In this contribution, we extend this previous algorithm to additionally change the nature of the element layer at the pore-grain interface to a cement phase instead of the original rock phase.

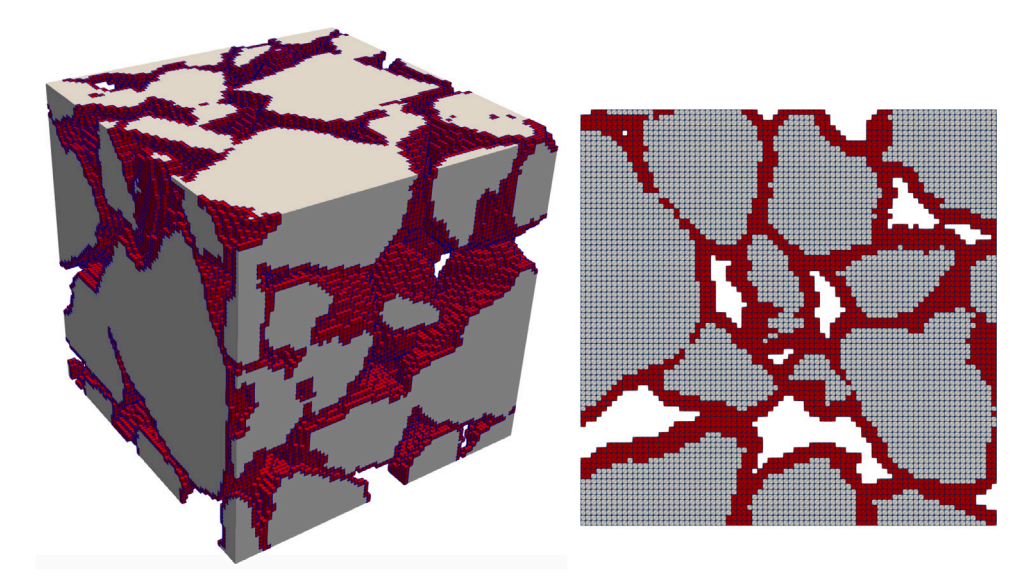


Fig. 7. (a) Visualisation of the digital rock with one cement layer in red. (b) Cross section of the digital rock after three steps of cementation. (For interpretation of the references to colour in this figure legend, the reader is referred to the web version of this article.)

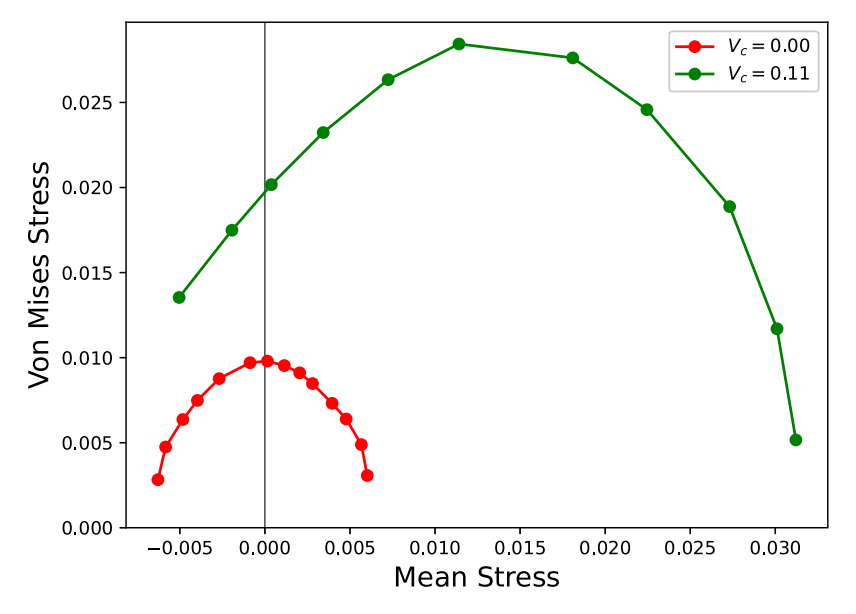


Fig. 8. Influence of one cement layer on the yield surface, using the sample of Fig. 7a.

The rock selected for cementation is a sandpack, which is an uncemented rock made of sand grains artificially consolidated. A cemented sandpack is similar to a sandstone in the sense that the cementation of a sandpack rock reproduces the natural diagenesis of a sandstone (Worden and Burley, 2009). A visual representation of the digital rock after running the algorithm once can be seen in Fig. 7a, with the cement layer coloured in red. In contrast to the rock phase, we consider the cement to obey a frictional-cohesive response, as typical in debonding approaches where the cement is undergoing brittle/shearing failure (Baek and Park, 2018). To this end, the cement is assumed to follow a Drucker–Prager yield criterion. Values of Young's modulus, cohesion and friction for the cement are discussed in the following sections. Due to the cement, we can observe in Fig. 8 that the cemented rock becomes pressure sensitive. The cemented rock also appears stronger which is the well-known consequence of cementation.

3.2. Influence of cementation volume

We first look at the influence of the volume of cementation V_c on the yield surface of the rock. Three levels of cementation are investigated, representing 11%, 21% and 28% of the total sample's volume and corresponding to the first three consecutive layers

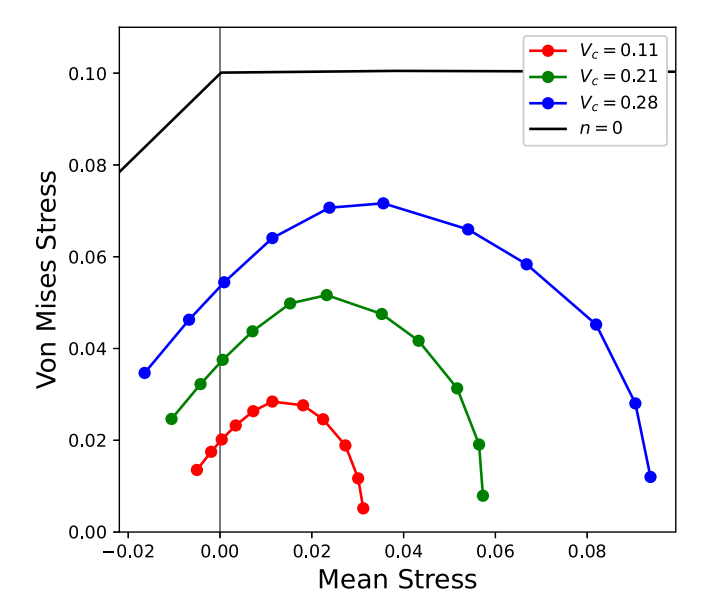


Fig. 9. Influence of increasing cementation volume on the yield surface.

of cementation following the methodology presented in Section 3.1. The corresponding yield surfaces of the cemented material are plotted in Fig. 9a. We observe that the increase of cementation does not change the macro-friction angle. However, the increase in cementation does result in an increase of strength. This is a verification of the expected behaviour of cementation (Bernabé et al., 1992; Yin and Dvorkin, 1994; den Brok et al., 1997), that we mentioned in the introduction.

We also derive the yield surface of the fully cemented rock for comparison. Since the two materials, grains and cement, are considered to have the same elastic properties in this section, the composite material at full cementation will experience the same stress in both phases. Therefore, the envelope will follow the minimum between the yield functions of the rock and cement phase. As seen in Fig. 9, the resulting yield surface follows the Drucker–Prager of the cement until it reaches q = 0.1 at which point it is capped by the J2 yield criterion of the grains. With increasing cementation volume, the total porosity of the material decreases and reaches zero at full cementation. We know from the theoretical study of Gurson (1977) that porosity is fundamentally responsible for the existence of the compaction cap. Hence, the fully cemented rock does not display a compaction cap anymore. This implies that the compaction cap of the partially cemented rock will stretch infinitely towards null porosity.

3.3. Influence of cement's mechanical properties

3.3.1. Young'S modulus

We start logically this subsection with elasticity, studying first the influence of the cement's rigidity on the yield surface. We assume that the cement cannot be more rigid than the grain skeleton ($\frac{E_g}{\sigma_0} = 200$). Therefore, we select three different of the cement's Young's modulus, $\frac{E_c}{\sigma_0} = 200$, 100 and 50. Using each of those, we compute the corresponding yield surface, which are all plotted in Fig. 10. The upscaled friction of the material does not change with elasticity. We can observe that a decrease of the cement's Young's modulus shifts the entire yield surface towards extension.

3.3.2. Cohesion

Moving on to plastic properties of the cement, we then study the influence of its cohesion C_c . Similarly to the elasticity, we assume that the cement cannot be stronger than the grains. Therefore, we decrease the cohesion starting from the strength of the grains, $C_c = 0.1$ to 0.025. The corresponding yield surfaces are plotted in Fig. 11. Once again, the macro-friction coefficient is not affected by the parameter studied. We can see that the yield surfaces are shrinking when decreasing the cement's cohesion. Counterintuitively, the cement's influence does not decrease when the cement is made weaker. Instead, it reduces the overall strength of the cemented material.

3.3.3. Friction

The last parameter studied is the cement's friction ϕ_c . We have already shown in Section 3.1 that the presence of a pressure-sensitive cement will turn the cemented material pressure-sensitive, with the appearance of a measurable macro-friction. In this section, we study more in details the effect of the parameter ϕ_c on the yield surface. Three angles are tested: 30, 45 and 80 degrees. The corresponding yield surfaces are plotted in Fig. 12. We can observe that ϕ_c directly affects the macro-friction and in turn, changes all the other parameters of the yield surface – macro-cohesion and isotropic compression yield pressure.

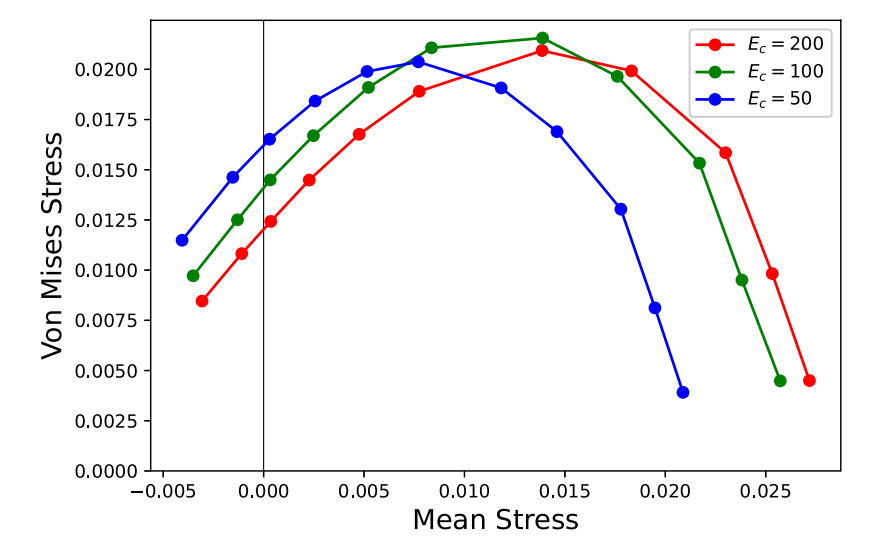


Fig. 10. Influence of the cement's Young's modulus.

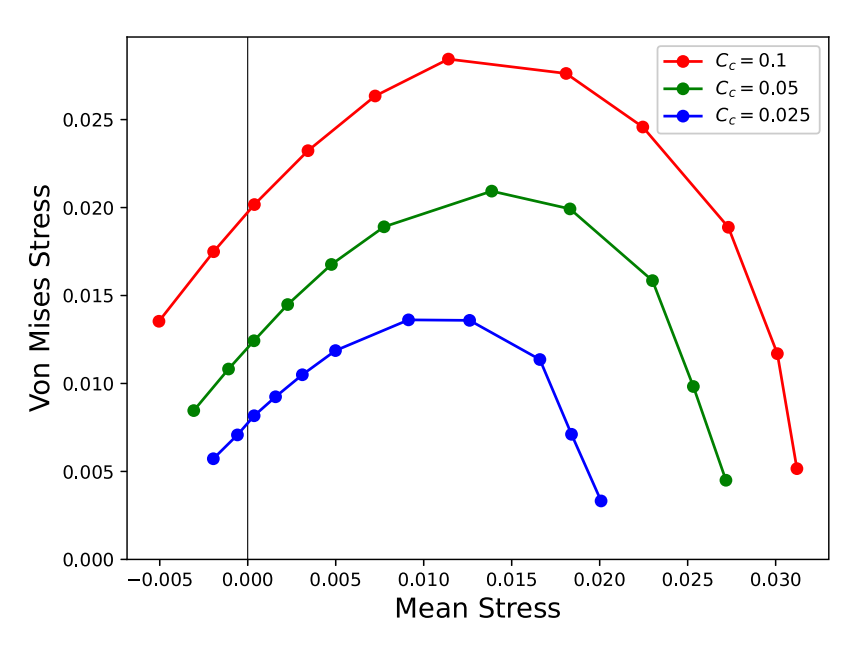


Fig. 11. Influence of the cement's cohesion.

4. Interpretation of results

In this section, we interpret and discuss the results of the parametric studies presented in the previous section.

4.1. Frictional part

It has been observed previously in this contribution that the cemented rock presents a Drucker Prager yield surface in the shearing regime, due to the presence of pressure sensitive cement. Except for the obvious exception of the study on the evolution of the cement's friction, all the different realisations produce the same macro-friction. Particularly, the macro-friction is the same for the fully cemented rock or for the one with only one layer of cement. This means that the macro-friction only depends on the rock and the cement's friction angle. This result is in agreement with experimental observations (Abdulla and Kiousis, 1997; Clough et al., 1981) that observed a change in the cohesion and not the friction angle by changing the cement content for cemented sand tested in a triaxial cell. Note that Lade and Overton (1989) have observed a change in the peak friction angle with the cement content, but

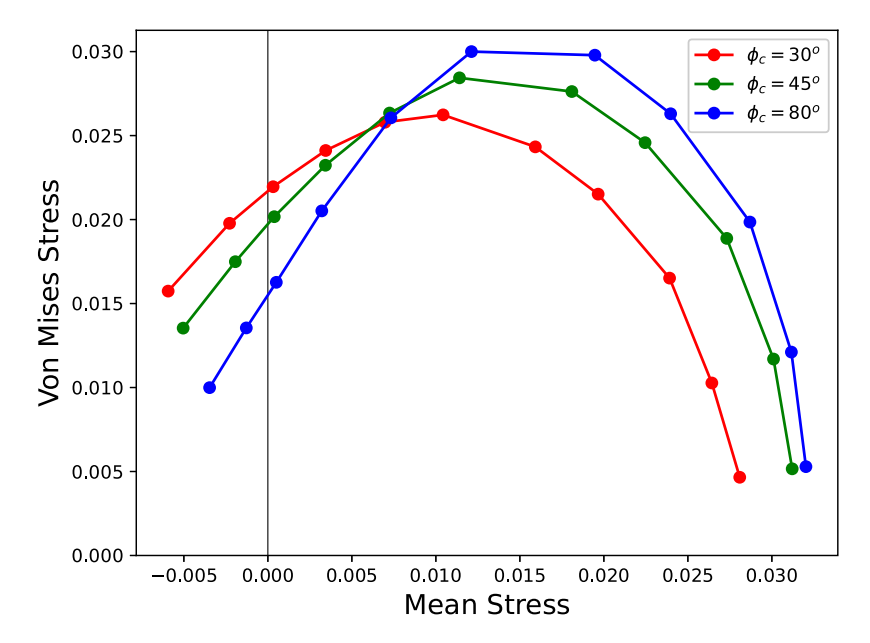


Fig. 12. Influence of the cement's friction angle.

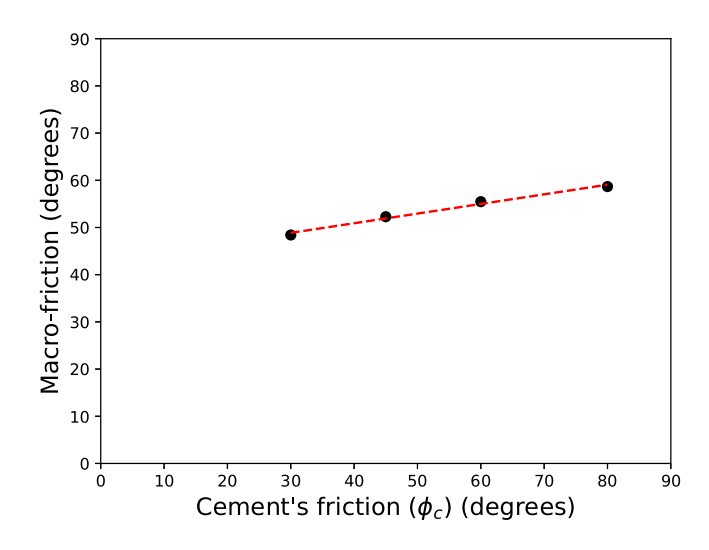


Fig. 13. Linear fitting of the macro-friction angle evolution with the cement's friction angle. The coefficient of determination of the linear regression is superior than 0.99.

this modification could be attributed to grain rearrangement close to the peak when bonds are damaged and the different amount of fines introduced for the different specimens with different cement contents.

Furthermore, we observe a linear evolution of the macro-friction angle with the cement's friction in Fig. 13.

In contrast, the macro-cohesion is varying in every realisation of the parametric studies. Fig. 14 summarises the evolution of the macro-cohesion for all the studies. It evolves non-linearly with increasing cementation volume until it reaches its maximum value at full cementation. The evolution is also nonlinear with the cement's Young's modulus. In this case, it is indeed more interesting to interpret the evolution of the yield surface as a horizontal translation as we pointed out in Section 3.3.1. Eventually, we only observe a linear evolution of the macro-cohesion with both the cement's cohesion and friction.

In summary, we found that the plastic properties of the cement (friction's angle, cohesion) have a direct, linear impact on the plastic properties of the cemented rock, in the frictional part.

4.2. Transition from frictional regime to compaction cap

From all the realisations shown in this contribution, we can clearly observe a transition from the Drucker Prager described in the previous section to the compaction cap. To be able to pinpoint with more precision where this transition occurs on the yield

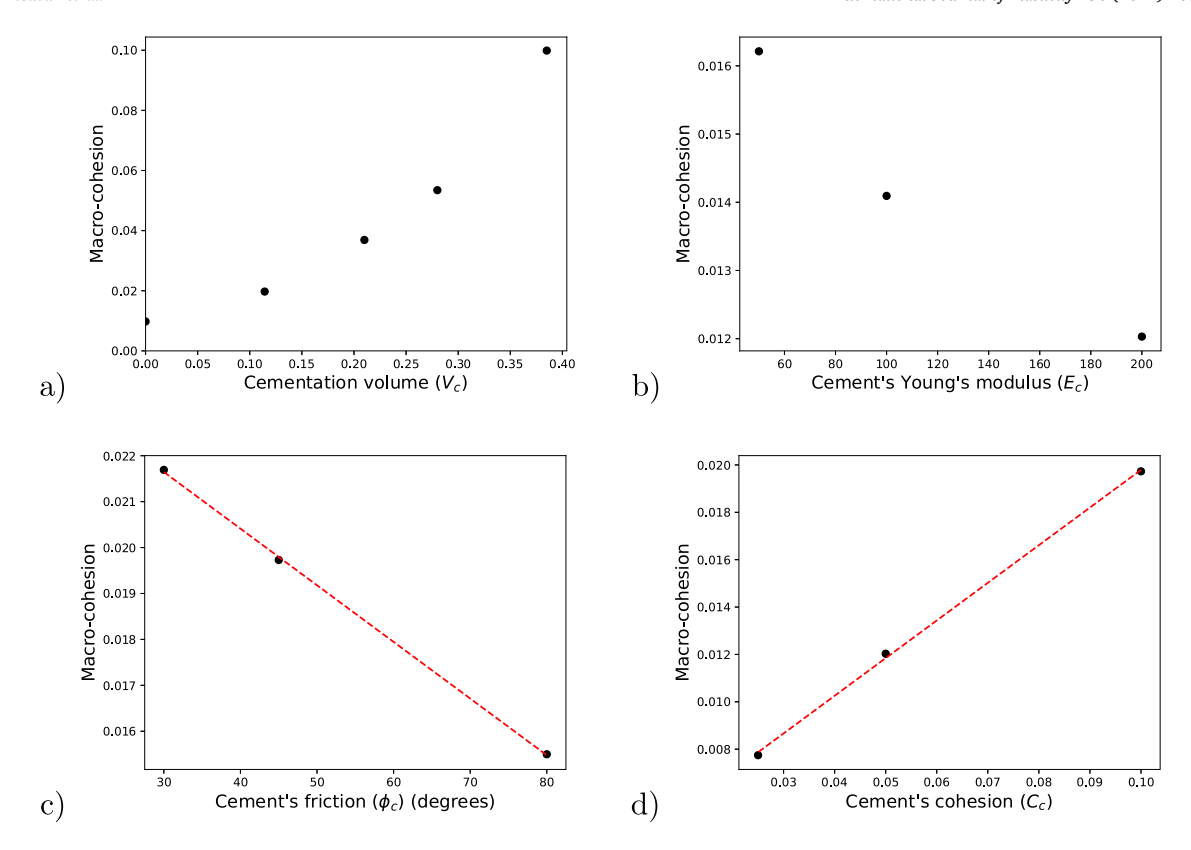


Fig. 14. Evolution of the macro-cohesion during the parametric study of Section 3.1. Linear regressions of (c) and (d) have a coefficient of determination superior than 0.999.

surface, we require a more quantitative assessment. We proceed to measure the evolution of the yield stress with the triaxial ratio angle θ (0° < θ < 180°), where the yield stress corresponds now to a distance from the origin r, as shown for an example in Fig. 15a.

In our parametric study, we observe that each point of the yield surface is aligned with the points on the other surfaces obtained with the same loading function. This is achieved on two conditions. The first one is that our loading paths all start from a null deviatoric and mean stress, as can be seen from Fig. 3a. The second is that the yield, corresponding to the limit of linear elasticity, does not deviate much from the stress-path of linear elasticity, as can be seen from Fig. 3b. A change of alignment would therefore only happen when the elastic properties of the sample are evolving during the study. Taking advantage of this interesting property resulting from our specific set-up, we understand that each loading function corresponds to one angle θ . For each loading function, we can therefore look at the evolution of the remaining varying polar coordinate r with the given studied parameter, which can be seen plotted for an example in Fig. 15b. In order to detect at the first order a qualitative change of behaviour, the evolution of r with a given parameter for a specified loading path is interpreted as a simple linear evolution with coefficients a and b. And by extracting the linear coefficient obtained for each loading function, we can finally plot its evolution in function of the angle θ in Fig. 16.

This method is quite compelling because originally each parametric study corresponds to a 3D data set, where each point is defined by p, q and the value of the parameter studied. By switching to polar coordinates r, θ and using an approximation of first order, we are able to reduce our data set to 2D, defined by the triaxial ratio angle θ and a linear coefficient a. This method finds a way of quantifying the evolution of the whole yield surface, which appreciation is otherwise completely subjective, and provide a simple 2D plot of the evolution in Fig. 16.

The results obtained with this methodology on every parametric study ran are presented in Fig. 16. We noted previously the restriction of having a constant linear elasticity and the limitation to a linear interpolation. In our parametric study on the cement's elasticity in Fig. 10, we can observe that the points at every angle θ are only slightly misaligned therefore we still consider the results obtained on this study, however with caution. With regards to the approximation of linear interpolation, we note first that the coefficient of determination R^2 is always above 0.95 in the frictional part. It was proven in the previous section that the macrocohesion is evolving linearly for most parameters of the study. This behaviour can be extended to the entire frictional part since we have shown that the frictional part of the yield surface corresponds to a Drucker Prager linear slope. The linear fit in the compaction cap is probably not adequate as the coefficient of determination drops below 0.9 but we believe that it still allows us to capture a qualitative description of the yield surface evolution.

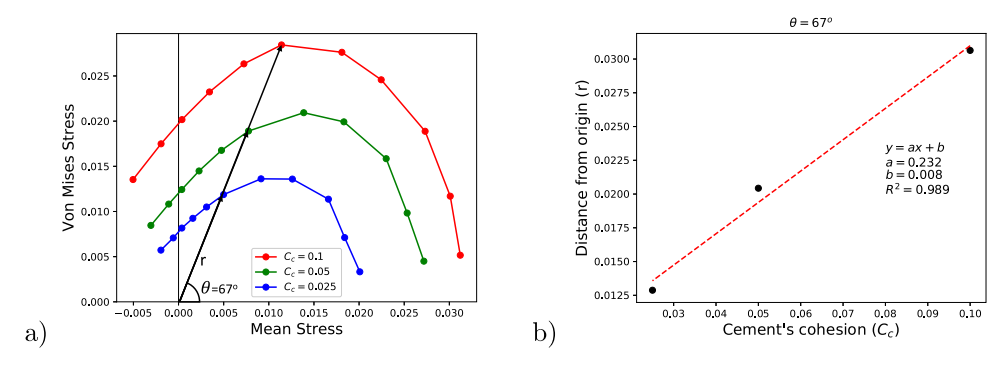


Fig. 15. Example of application of the linear scaling method for the cement's cohesion study. (a) Each yield point can be determined by its distance to the origin r and a triaxial ratio angle θ which corresponds for our set-up to a given loading function. (b) For each triaxial ratio angle θ , the evolution of r with the parameter studied can be interpolated by a linear function.

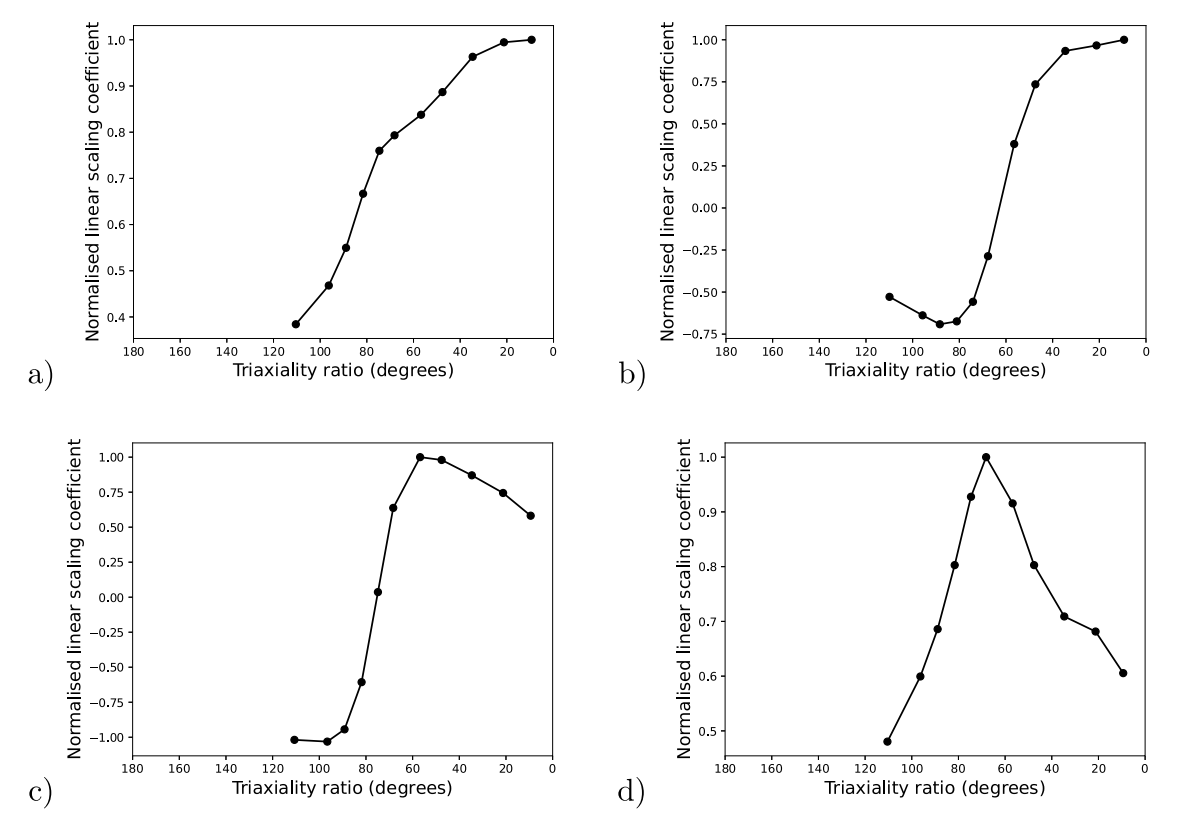


Fig. 16. Evolution of the linear scaling coefficient with the triaxial ratio angle computed with the methodology explained in Section 4.2, for the different parametric studies of Section 3.1: (a) Cementation volume (b) Young's modulus (c) Cohesion (d) Friction angle. The linear scaling coefficients are normalised by their respective maximum value.

All the plots from Fig. 16 present a change of behaviour between two regimes. This transition is the most clearly observed in Fig. 16d and corresponds to an angle of 67°. We note that the results is only approximate as it is subject to the discretisation of the yield surface. This angle value is confirmed in the rest of the plots where the same angle corresponds to a change of behaviour from a predominantly dilatant shear failure at low-confinements to compacting shear failure at higher confinements. At the transitional angle of 67° the material seems to deform in an incompressible way, in a response akin to the critical state typically observed in porous media (Wood, 1990). While this angle value, separating dilatant shear failure to compactive shear failure, can remind of the critical state line, it needs to be noted though, that in our case the transition is not always correlated with the peak deviator stress, owing to the presence of the soft cement.

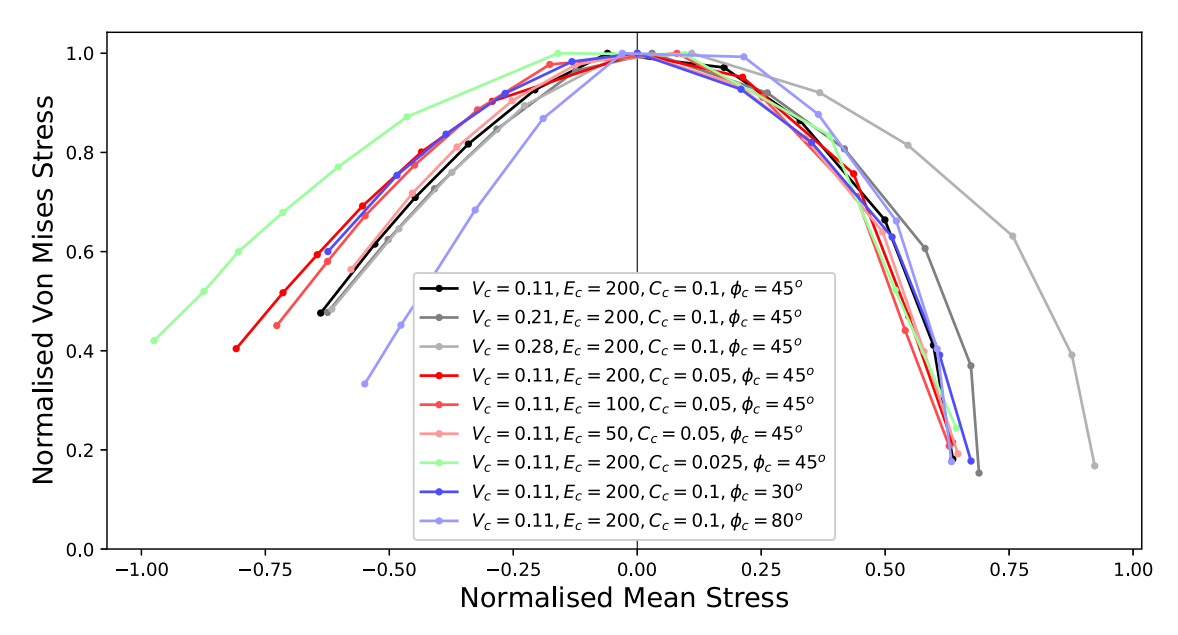


Fig. 17. Superposition of the compaction caps of all realisations from the parametric study of Section 3.1, normalised by their respective peak stress.

4.3. Compaction cap

Around the angle found in the previous section, we can clearly observe the yield surfaces transitioning from the shearing regime with a Drucker Prager to the compaction with a cap. This compaction cap is present already for the uncemented rock as it exists as soon as the porosity is non null. From the study in the previous section, we discovered that the compaction cap is not expanding linearly from the origin. Because the compaction cap starts from a different point of transition, studied in the previous section, it is difficult to visually interpret the evolution of the shape of the compaction cap. For this reason, we first proceed to a normalisation of all the compaction caps. The value chosen for the normalisation is the peak stress of the yield surface, a bit before which the compaction cap already starts appearing. The normalised yield surfaces are then translated so that the peak stress value corresponds to the origin of the normalised mean stress. The result for all the realisations from the parametric studies of Section 3.1 are superposed on the same plot, Fig. 17. To our surprise, the compaction caps that looked all different now display the same shape and fall on top of each other after the normalisation, with the exception of the rocks cemented with additional layers of cement. In this specific case, we have shown that the isotropic compression yield pressure will tend to stretch infinitely. While Fig. 9 could only lead us to this interpretation, it is now visually confirmed in Fig. 17 as we see the grey normalised yield surfaces stretching open.

The conclusion of this study is that the compaction cap shape does not depend on the cement's mechanical properties. It is however scaled, to be a transition of the frictional part. Instead, the compaction cap shape depends solely on the microstructure which also explains why the shape is changing for increasing cementation volume as this precipitation of cement changes the microstructure. This result concurs with Gurson (1977) that formulated a generic yield criterion (consisting of a pure compaction cap in his case) depending solely of the medium's porosity, scaled with a reference stress.

Linking all parts together, the yield surface macro-friction and macro-cohesion can be determined from the simple relationships they have with the cement's properties, determined in Section 4.1. The transition point from the frictional regime is found from the intersection of the friction slope with the line leaving the origin of the graph at the angle established in Section 4.2. Starting from the point, we can fit the compaction cap, scaled to the transition point, which shape has been determined in Section 4.3. Eventually, it appears that our interpretation provides a full modelling of the cemented yield surface.

5. Comparison with existing models and experimental data

In this section we place back our study in the context of existing literature and compare our results with existing models or experimental data.

5.1. Theoretical yield criteria

As discussed in the introduction, the determination of the yield surface of porous materials in material science is primarily done with theoretical yield criteria, derived on idealised model of porous materials. The most common one is Gurson's criterion (Gurson, 1977) derived on the hollow sphere model. Gurson had only interest only in metallic materials. Therefore, he considered a von Mises

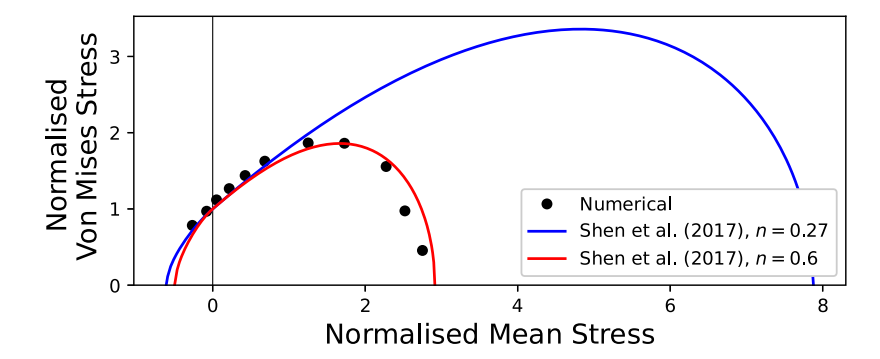


Fig. 18. Comparison of the yield surface obtained by the analytical expression of Shen et al. (2017) for two different porosities and the yield points obtained numerically ($V_c = 0.11$, $\phi_c = 45^\circ$ and $C_c = 0.025$). Yield surface stresses are normalised by their respective macro-cohesion.

yield criterion for the microstructure which resulted in a pure compaction cap similarly obtained in our study for the uncemented rock skeleton, shown for example in Fig. 8. In order to compare a Gurson type model with our data generated for cemented materials, we select one of the extension of Gurson's criterion, which considers a Drucker–Prager yield surface for the microstructure. The model was developed by Shen et al. (2017) and is expressed as:

$$q_y^2 = \left(-2n\cosh\left(\frac{2M - Sign(p_y)}{2M}ln(1 + 3Mp_y)\right) + 1 + n^2\right)\left(1 + \frac{3Mp_y}{1 - n}\right)^2 \tag{9}$$

with M is the pressure sensitivity coefficient which is physically related to the internal friction angle of solid matrix ϕ_c by $M = tan(\phi_c)/3$, and n is the porosity of the porous medium.

In Fig. 18 is plotted one of the yield surface previously computed in Section 3 ($V_c = 0.11$ which corresponds to a porosity of 0.27, $\phi_c = 45^\circ$ and $C_c = 0.025$) against Eq. 9, calculated for the same porosity of the cemented sample and using a macro-friction calibrated on the macroscopic response of the digital rock. Both models are normalised by their respective cohesion for the sake of comparison. While the frictional parts are matching well, the compaction caps are not. The analytical expression from Shen et al. (2017) extends further than the one of our digital rock, meaning that the model predicts the rock to be stronger in compaction. This can be easily understood by the difference of structures that the two yield surfaces correspond to. Compared to the rock microstructure, highly heterogeneous and yielding quickly at the contact point between grains, the homogeneous hollow sphere has no localised points of weakness and is therefore more resistant. Interestingly, this influence of structure shape has been pointed out already by Tvergaard and Needleman (1984), soon after the publication of Gurson's criterion (Gurson, 1977). To solve for this difference of what they refer to as "void shape", their proposed model includes a shape coefficient "X" by which the porosity is multiplied. When applying such concept to Eq. 9, i.e. replacing the porosity by an effective porosity, we can now find a value of the shape coefficient that fits the compaction much better, as seen in Fig. 18 and the value of the void shape coefficient used here is approximately 2.2. Note that this match means that the yielding of our digital rock structure is equivalent to the one of a hollow sphere with an effective porosity of 60%, showing how much more resistant this idealised model is, in comparison to a real rock microstructure. This particularly good fit proves that idealised models can capture the correct mechanical behaviour of yielding of porous materials. Nonetheless, the existence this shape coefficient emphasises the necessity to use direct numerical simulations in order to quantify the influence of the exact microstructure.

5.2. Asymmetric Cam-Clay model

We consider the analytical expression introduced by Samudio (2017), denominated as the asymmetric Cam-Clay model that defines the yield surface expressed in the invariants von Mises and mean pressure space. This model presents several important features compared to the numerous yield surfaces existing in the literature, namely: isotropic caps at both traction and compression with vertical tangents, a flexible contractant-dilatant behaviour and real function values for all real stress states. The mathematical expression of the yield surface is similar to the classical modified Cam-Clay model and introduces an additional parameter that allows to break the symmetry of an ellipse and tend to a yield surface that is closer a Drucker-Prager at low confining pressure and a cap for higher pressures. Compared to the analytical expression of Eq. 9, this model does not use parameters of the microstructure, but macroscopic parameters like the yield pressure in isotropic traction and compression that are easier to assess from experimental characterisations. In this case, a fit of the numerical results from Section 3 with this model would allow us to obtain the evolution of these experimental parameters with the cement properties. The expression is:

$$q_{y} = \sqrt{M^{2}(p_{c} - p_{y})(p_{y} + p_{t})e^{-k\frac{(2p_{y} + p_{t} - p_{c})}{(p_{t} + p_{c})}}}$$
(10)

where k is a parameter that controls the asymmetry of the yield surface, p_c and p_t are the yield pressures of isotropic compression and traction respectively. Note that when k = 0 and $p_t = 0$, we retrieve the symmetric modified Cam-Clay model. M is a parameter that

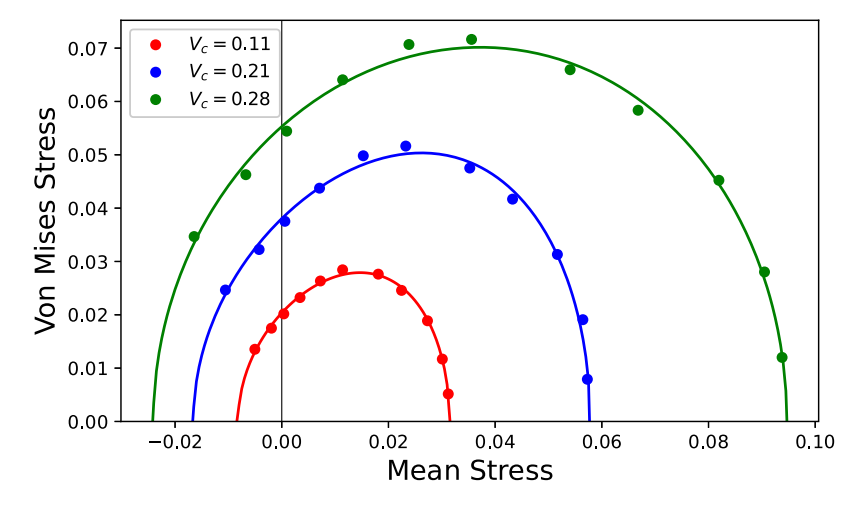


Fig. 19. Fit of yield surfaces obtained numerically for different volume of cement in Fig. 9 (points) with the asymmetric Cam-Clay model (full line).

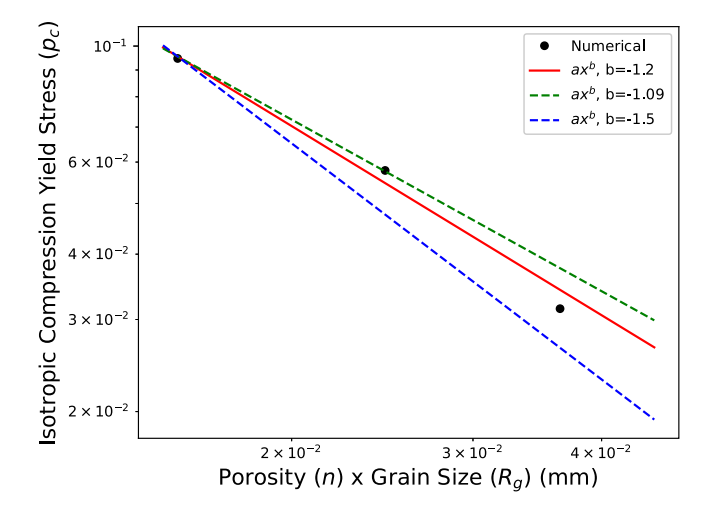


Fig. 20. Plot in logarithmic scale of the isotropic compression yield stress (p_c) as a function of porosity (n) ×grain size (R_g) from the numerical data of the influence of the cementation volume fitted with the asymmetric Cam-Clay model in Fig. 19 (points) compared with the best fit obtained by the least-square method (full line) and experimental observations (dashed lines).

controls the height of the yield surface in the q_y -direction of the p_y-q_y space. The surface is determined by the 4 parameters k, p_c , p_t and M which define a full yield surface, including the frictional part and the compaction cap, with a single equation instead of one for each regime, as commonly found in the literature (Wong et al., 1997). This model therefore allows for a continuous transition between regime which is more realistic. Specifically, the model has been shown to fit well the full yield surface for carbonate rocks (Abdallah, 2019). In Fig. 19, the yield surfaces obtained numerically for different volumes of cement are successfully fitted by the asymmetric Cam-Clay model, using nonlinear global optimisation.

As a parameter extracted from the model during the fitting exercise, we can access the evolution of the isotropic compression yield pressure p_c , characterising the cap, with the cementation volume V_c . It has been shown experimentally that p_c follows a power law of the product of initial porosity n and grain radius R_g . Wong et al. (1997) found the exponent to be equal to -1.5, but a recent study integrating more data from the literature found a lower value of -1.09 (Rutter and Glover, 2012). These values can be compared with the one we calculate from the p_c values extracted from our fit with Eq. (10) in Fig. 19. For that, we consider a mean grain radius of 0.125 mm for the LV60 A sandpack (Talabi et al., 2009). Note that as the cementation volume increases, the grain size increases as well. We take this effect into account by adding to R_g for each level of cementation the value of the layer thickness which corresponds to one grid voxel with our erosion algorithm. The results of the comparison are plotted in Fig. 20, in logarithmic scale for a clear assessment of the power law which appears as a linear slope in this scale. The exponent fitted on our numerical results equals -1.2 which is close to the value found by Rutter and Glover (2012), showing a good agreement of our numerical simulations with experimental observations.

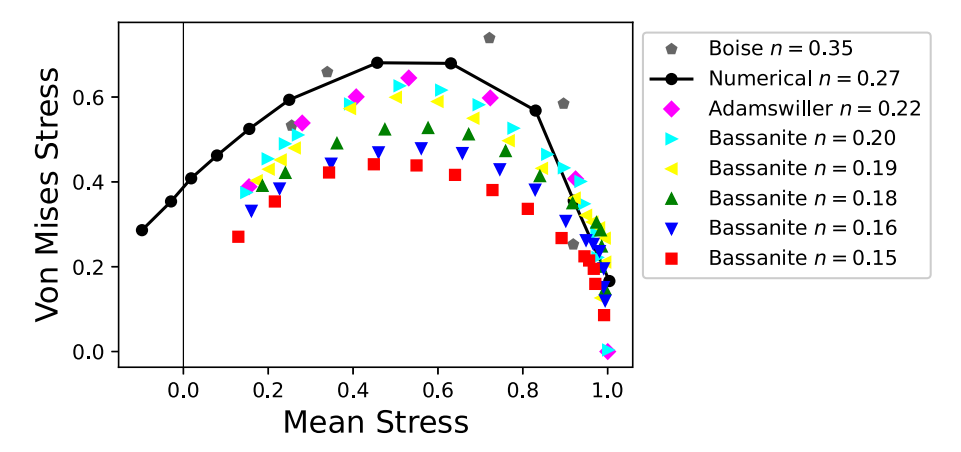


Fig. 21. Comparison between yield surfaces obtained experimentally for Bassanite (Bedford et al., 2018) and sandstone (Wong et al., 1997), and a yield surface obtained numerically in our study. All datasets are normalised by their respective isotropic compression yield pressure.

5.3. Experiments

In order to broaden comparisons of the yield surface computed with our method, we consider real observations obtained experimentally using a triaxial apparatus. Bedford et al. (2018) have performed conventional triaxial experiments at different confining pressures on porous Bassanite, a material formed from the dehydration of gypsum. They have obtained the yield surface for different porosities of this material. One of our yield surface is plotted alongside their data in Fig. 21. Note that we selected the yield surface that best compares to Bedford's data as no data on the mechanical behaviour of the cement or grains individually is available. It corresponds to the yield surface produced in Section 3.3.2. Its parameters for the cement are $E_c = 200$, $C_c = 0.025$ and $\phi_c = 45^{\circ}$ and its porosity is 0.27. All datasets are normalised by their respective isotropic compression yield pressure in order to compare only the shapes of the yield surfaces. We can observe in the experimental data for Bassanite that the increase of the porosity induces an increase of the maximum normalised von Mises stress reached by the yield surface. Our yield surface also follows this trend and lies higher than Bedford's data that has a lower porosity. While there is limited experimental data in the frictional regime, we can extrapolate that the friction angle is quite similar to our simulated yield surface.

Instead of Bassanite, the cemented microstructure generated by using our numerical erosion algorithm on a sandpack rock would undoubtedly be closer to the one of a sandstone. Therefore, we also add data of two different sandstones on Fig. 21: Adamswiller with a porosity of 0.22 and Boise II with a porosity of 0.35 (Wong et al., 1997). We can observe that the yield surface from our numerical study lies in between the real data of these two sandstones, in accordance with the trend unveiled by Bedford et al. (2018). The resemblance of our yield surfaces, obtained from direct simulation on the microstructure, with the real ones, obtained traditionally from destructive triaxial tests, increases the level of confidence about our modelling of macroscopic yielding of cemented materials.

6. Conclusion

This contribution introduced a numerical method to homogenise the yield surfaces of rocks. Based on simulations of elasto-plastic mechanical loadings on digital rocks, the full yield surface, both in compression and in tension, can be upscaled. The yield surfaces produced are shown to reproduce the shape obtained in experiments and, oppositely, match as well the more theoretical yield criteria developed for porous materials. This framework allows for the study of the rock microstructure's influence on its yield. We found that this complex structure is weaker in comparison to the single spherical pore structure. For this reason, theoretical yield criteria on idealised pore models end up overestimating the strength of rocks. This aspect legitimise the usage of direct numerical simulations to estimate the yield surface of rocks instead of structure-agnostic criteria.

One advantage of this numerical method is to be able to easily follow the evolution of the yield surface from the variation of arbitrarily chosen parameters. This is particularly suited to study dynamical processes such as the one chosen in this contribution, cementation. Using this feature, we could first verify that rock strength increases during cementation, due to an accumulation of cement at the pore-grain interface. Furthermore, new trends were discovered that link the yield surface shape properties with the cement's mechanical properties. Cement stiffness only translates the yield surface along the mean stress axis. In the frictional regime, linear relationships were found between the cement's plastic parameters (cohesion, friction) and the plastic parameters of the macroscopic response. The existence of a clear separatrix between the frictional and compaction regime was established. We expect this to correspond to the critical state line but only a further investigation on the matter can confirm this assumption. Finally, we determined that the shape of the compaction cap can solely be attributed to the rock microstructure and does not depend on the cement mechanical properties. This last result can prove particularly useful for the quantitative estimation of a rock yield surface. Indeed, only the isotropic compression yield pressure needs to be determined in supplement to the compaction cap numerically computed on the μ CT scans of the rock to be able to evaluate the real compaction cap of this rock.

As demonstrated, implementing a rigorous homogenisation procedure is not trivial. Particularly, one needs to be careful about respecting Hill's lemma which requires specific boundary conditions and a proper averaging of stresses and strain. However, more representativeness is eventually achieved compared to surface averaging in standard experimental set-up. While this study remained qualitative for the single purpose to uncover a few mechanical trends, we still pointed out one strong requirement necessary for quantitative estimation of the rock yield surface, which is the consideration of a sample larger than the REV size. In our study, it was shown that the REV size would only be reached with a bigger sample than considered. At the given REV size, the problem then remains the usual compromise of the digital rock modeller between resolution and computational cost.

This paper illustrated non-exhaustively the innovative capabilities linked to our method of yield surface homogenisation of a digital rock. With it, we hope to better understand the shape of rock yield surfaces and be able to attribute some of its features to mechanical properties or morphological parameters. Going further than characterisation, this study on cementation can be of interest for civil engineering design in the novel field where material strength is optimised using a bio-cementation process (Cui et al., 2017; Iqbal et al., 2021). Still, cementation served as an example to study processes affecting the yield surface by altering the microstructure but the list can be extended to many more, namely hydraulic, mechanical, chemical or thermal. The upscaling of the yield surface should be considered as a first step towards the upscaling of the entire plastic behaviour. Indeed, it requires simulation of some plastic deformation, to reach the macroscopic yield. Such framework opens the door to further homogenisation of macroscopic plastic properties and therefore to an extension of Digital Rock Physics towards including more geomechanics.

CRediT authorship contribution statement

Martin Lesueur: Conceptualization, Methodology, Software, Investigation, Writing. Manolis Veveakis: Conceptualization, Methodology, Writing. Hadrien Rattez: Conceptualization, Methodology, Investigation, Writing.

Declaration of competing interest

The authors declare that they have no known competing financial interests or personal relationships that could have appeared to influence the work reported in this paper.

Acknowledgements

This work was supported by computational resources provided by the Pawsey Supercomputing Centre with funding from the Australian Government and the Government of Western Australia and the Consortium des Équipements de Calcul Intensif (CÉCI), funded by the Fonds de la Recherche Scientifique de Belgique (F.R.S.-FNRS) under Grant No. 2.5020.11 and by the Walloon Region. M.V. acknowledges support by the DE-NE0008746-DoE and NSF-CMMI-2042325 United States projects.

References

Abdallah, Y., 2019. Compaction Banding in High-Porosity Limestones: Experimental Observations and Modelling (Ph.D. thesis). Universite Paris-Est. Abdulla, A.A., Kiousis, P.D., 1997. Behavior of cemented sands—I. Testing. Int. J. Numer. Anal. Methods Geomech. 21 (8), 533–547. http://dx.doi.org/10.1002/(sici)1096-9853(199708)21:8<533::aid-nag889>3.0.co;2-0.

Andrä, H., Combaret, N., Dvorkin, J., Glatt, E., Han, J., Kabel, M., Keehm, Y., Krzikalla, F., Lee, M., Madonna, C., Marsh, M., Mukerji, T., Saenger, E.H., Sain, R., Saxena, N., Ricker, S., Wiegmann, A., Zhan, X., 2013. Digital rock physics benchmarks—part I: Imaging and segmentation. Comput. Geosci. 50, 25–32. http://dx.doi.org/10.1016/j.cageo.2012.09.005.

Arns, C.H., Knackstedt, M.A., Pinczewski, W.V., Garboczi, E.J., 2002. Computation of linear elastic properties from microtomographic images: Methodology and agreement between theory and experiment. Geophysics 67 (5), 1396–1405. http://dx.doi.org/10.1190/1.1512785.

Arns, C.H., Knackstedt, M.A., Pinczewski, W., Martys, N.S., 2004. Virtual permeametry on microtomographic images. J. Pet. Sci. Eng. 45 (1–2), 41–46. http://dx.doi.org/10.1016/j.petrol.2004.05.001.

Baek, H., Park, K., 2018. Cohesive frictional-contact model for dynamic fracture simulations under compression. Int. J. Solids Struct. 144–145, 86–99. http://dx.doi.org/10.1016/j.ijsolstr.2018.04.016.

Bedford, J.D., Faulkner, D.R., Leclère, H., Wheeler, J., 2018. High-resolution mapping of yield curve shape and evolution for porous rock: The effect of inelastic compaction on porous bassanite. J. Geophys. Res. Solid Earth 123 (2), 1217–1234. http://dx.doi.org/10.1002/2017jb015250.

Bernabé, Y., Fryer, D.T., Hayes, J.A., 1992. The effect of cement on the strength of granular rocks. Geophys. Res. Lett. 19 (14), 1511–1514. http://dx.doi.org/10.1029/92g101288.

 $Besson,\ J.,\ 2009.\ Continuum\ models\ of\ ductile\ fracture:\ A\ review.\ Int.\ J.\ Damage\ Mech.\ 19\ (1),\ 3-52.\ http://dx.doi.org/10.1177/1056789509103482.$

Bienawski, Z., 1974. Estimating the strength of rock materials. J. South Afr. Inst. Min. Metall..
Blunt, M.J., Bijeljic, B., Dong, H., Gharbi, O., Iglauer, S., Mostaghimi, P., Paluszny, A., Pentland, C., 2013. Pore-scale imaging and modelling. Adv. Water Resour.

Blunt, M.J., Bljeljic, B., Dong, H., Gharbi, O., Iglauer, S., Mostagnimi, P., Paruszny, A., Pentiand, C., 2013. Pore-scale imaging and modelling. Adv. water Resour. 51, 197–216. http://dx.doi.org/10.1016/j.advwatres.2012.03.003.

den Brok, S.W., David, C., Bernabé, Y., 1997. Preparation of synthetic sandstones with variable cementation for studying the physical properties of granular rocks. C. R. Acad. Sci.-Ser. IIA - Earth Planet. Sci. 325 (7), 487–492. http://dx.doi.org/10.1016/s1251-8050(97)89866-7.

Cao, Y., Shen, W., Burlion, N., Shao, J., 2018. Effects of inclusions and pores on plastic and viscoplastic deformation of rock-like materials. Int. J. Plast. 108, 107–124. http://dx.doi.org/10.1016/j.ijplas.2018.04.015.

Chen, W.-F., 1975. Limit Analysis and Soil Plasticity. In: Developments in Geotechnical Engineering, vol. 7, Elsevier Scientific Pub. Co..

Clough, G.W., Sitar, N., Bachus, R.C., Rad, N.S., 1981. Cemented sands under static loading. J. Geotech. Eng. Div. 107 (6), 799–817. http://dx.doi.org/10.1061/ajgeb6.0001152.

Cnudde, V., Boone, M., 2013. High-resolution X-ray computed tomography in geosciences: A review of the current technology and applications. Earth-Sci. Rev. 123, 1–17. http://dx.doi.org/10.1016/j.earscirev.2013.04.003.

Cui, M.-J., Zheng, J.-J., Zhang, R.-J., Lai, H.-J., Zhang, J., 2017. Influence of cementation level on the strength behaviour of bio-cemented sand. Acta Geotech. 12 (5), 971–986. http://dx.doi.org/10.1007/s11440-017-0574-9.

- Cundall, P.A., Strack, O.D.L., 1979. A discrete numerical model for granular assemblies. Géotechnique 29 (1), 47–65. http://dx.doi.org/10.1680/geot.1979.29.1.47. Delenne, J.-Y., Topin, V., Radjai, F., 2009. Failure of cemented granular materials under simple compression experiments and numerical simulations. Acta Mech. 205 (1–4), 9–21. http://dx.doi.org/10.1007/s00707-009-0160-9.
- Drucker, D.C., Prager, W., 1952. Soil mechanics and plastic analysis or limit design. Quart. Appl. Math. 10 (2), 157–165. http://dx.doi.org/10.1090/qam/48291. Dvorkin, J., Armbruster, M., Baldwin, C., Fang, Q., Derzhi, N., Gomez, C., Nur, B., Nur, A., 2008. The future of rock physics: computational methods vs. lab testing. First Break 26 (9), http://dx.doi.org/10.3997/1365-2397.26.1292.28600.
- Dvorkin, J., Derzhi, N., Diaz, E., Fang, Q., 2011. Relevance of computational rock physics. Geophysics 76 (5), E141–E153. http://dx.doi.org/10.1190/geo2010-0352.1.
- Estrada, N., Taboada, A., 2013. Yield surfaces and plastic potentials of cemented granular materials from discrete element simulations. Comput. Geotech. 49, 62–69. http://dx.doi.org/10.1016/j.compgeo.2012.11.001.
- Fritzen, F., Forest, S., Böhlke, T., Kondo, D., Kanit, T., 2012. Computational homogenization of elasto-plastic porous metals. Int. J. Plast. 29, 102–119. http://dx.doi.org/10.1016/j.ijplas.2011.08.005.
- Gao, F., Kang, H., 2017. Grain-based discrete-element modeling study on the effects of cementation on the mechanical behavior of low-porosity brittle rocks. Int. J. Geomech. 17 (9), 04017061. http://dx.doi.org/10.1061/(asce)gm.1943-5622.0000957.
- Gao, X., Zhang, T., Zhou, J., Graham, S.M., Hayden, M., Roe, C., 2011. On stress-state dependent plasticity modeling: Significance of the hydrostatic stress, the third invariant of stress deviator and the non-associated flow rule. Int. J. Plast. 27 (2), 217–231. http://dx.doi.org/10.1016/j.ijplas.2010.05.004.
- Gens, A., Nova, R., 1993. Conceptual bases for a constitutive model for bonded soils and weak rocks. In: Geotechnical Engineering of Hard Soils-Soft Rocks. pp. 485–494.
- Gologanu, M., Leblond, J.-B., Devaux, J., 1993. Approximate models for ductile metals containing non-spherical voids—Case of axisymmetric prolate ellipsoidal cavities. J. Mech. Phys. Solids 41 (11), 1723–1754. http://dx.doi.org/10.1016/0022-5096(93)90029-f.
- Guével, A., Rattez, H., Veveakis, E., 2020. Viscous phase-field modeling for chemo-mechanical microstructural evolution: application to geomaterials and pressure solution. Int. J. Solids Struct. 207, 230–249. http://dx.doi.org/10.1016/j.ijsolstr.2020.09.026.
- Gurson, A., 1977. Continuum theory of ductile rupture by void nucleation and growth: Part I—Yield criteria and flow rules for porous ductile media. J. Eng. Mater. Technol. 99 (1), 2–15. http://dx.doi.org/10.1115/1.3443401.
- Hill, R., 1963. Elastic properties of reinforced solids: Some theoretical principles. J. Mech. Phys. Solids 11 (5), 357–372. http://dx.doi.org/10.1016/0022-5096(63)90036-x.
- Huang, J.T., Airey, D.W., 1998. Properties of artificially cemented carbonate sand. J. Geotech. Geoenviron. Eng. 124 (6), 492–499. http://dx.doi.org/10.1061/(asce)1090-0241(1998)124:6(492).
- Hueckel, T., Pellegrini, R., 2002. Reactive plasticity for clays: application to a natural analog of long-term geomechanical effects of nuclear waste disposal. Eng. Geol. 64 (2–3), 195–215. http://dx.doi.org/10.1016/s0013-7952(01)00114-4.
- Imperial College Consortium On Pore-Scale Modelling, 2014. LV60a sandpack. http://dx.doi.org/10.6084/m9.figshare.1153795.
- Iqbal, D.M., Wong, L.S., Kong, S.Y., 2021. Bio-cementation in construction materials: A review. Materials 14 (9), 2175. http://dx.doi.org/10.3390/ma14092175. Jaeger, J.C., 2007. Fundamentals of Rock Mechanics. Wiley-Blackwell, ISBN: 0632057599.
- Kawamoto, R., Andò, E., Viggiani, G., Andrade, J.E., 2018. All you need is shape: Predicting shear banding in sand with LS-DEM. J. Mech. Phys. Solids 111, 375–392. http://dx.doi.org/10.1016/j.jmps.2017.10.003.
- Lade, P.V., Overton, D.D., 1989. Cementation effects in frictional materials. J. Geotech. Eng. 115 (10), 1373–1387. http://dx.doi.org/10.1061/(asce)0733-9410(1989)115:10(1373).
- Leclerc, J., Nguyen, V.-D., Pardoen, T., Noels, L., 2020. A micromechanics-based non-local damage to crack transition framework for porous elastoplastic solids. Int. J. Plast. 127, 102631. http://dx.doi.org/10.1016/j.ijplas.2019.11.010.
- Leroueil, S., Vaughan, P.R., 1990. The general and congruent effects of structure in natural soils and weak rocks. Géotechnique 40 (3), 467–488. http://dx.doi.org/10.1680/geot.1990.40.3.467.
- Lesueur, M., 2020. Influence of Multiphysics Couplings Across Scales: from Digital Rock Physics to Induced Fault Reactivation (Ph.D. thesis). UNSW Sydney, http://dx.doi.org/10.26190/unsworks/21844.
- Lesueur, M., Casadiego, M.C., Veveakis, M., Poulet, T., 2017. Modelling fluid-microstructure interaction on elasto-visco-plastic digital rocks. Geomech. Energy Environ. 12, 1–13. http://dx.doi.org/10.1016/j.gete.2017.08.001.
- Lesueur, M., Poulet, T., Veveakis, M., 2020a. Permeability hysteresis from microchannels opening during dissolution/reprecipitation cycle. Geophys. Res. Lett. 47 (18), http://dx.doi.org/10.1029/2020gl088674.
- Lesueur, M., Poulet, T., Veveakis, M., 2020b. Three-scale multiphysics finite element framework (FE3) modelling fault reactivation. Comput. Methods Appl. Mech. Engrg. 365, 112988. http://dx.doi.org/10.1016/j.cma.2020.112988.
- Lesueur, M., Poulet, T., Veveakis, M., 2021. Predicting the yield strength of a 3D printed porous material from its internal geometry. Addit. Manuf. 44, 102061. http://dx.doi.org/10.1016/j.addma.2021.102061.
- Liang, J., Gurevich, B., Lebedev, M., Vialle, S., Yurikov, A., Glubokovskikh, S., 2020. Elastic moduli of arenites from microtomographic images: A practical digital rock physics workflow. J. Geophys. Res. Solid Earth 125 (10), http://dx.doi.org/10.1029/2020jb020422.
- Liu, J., Sarout, J., Zhang, M., Dautriat, J., Veveakis, E., Regenauer-Lieb, K., 2017. Computational upscaling of drucker-prager plasticity from micro-CT images of synthetic porous rock. Geophys. J. Int. 212 (1), 151–163. http://dx.doi.org/10.1093/gji/ggx409.
- Madou, K., Leblond, J.-B., 2012. A gurson-type criterion for porous ductile solids containing arbitrary ellipsoidal voids—I: Limit-analysis of some representative cell. J. Mech. Phys. Solids 60, 1020–1036.
- Meade, E.D., Sun, F., Tiernan, P., O'Dowd, N.P., 2021. A multiscale experimentally-based finite element model to predict microstructure and damage evolution in martensitic steels. Int. J. Plast. 139, 102966. http://dx.doi.org/10.1016/j.iiplas.2021.102966.
- Mostaghimi, P., Blunt, M.J., Bijeljic, B., 2012. Computations of absolute permeability on micro-CT images. Math. Geosci. 45 (1), 103–125. http://dx.doi.org/10. 1007/s11004-012-9431-4.
- Mousavi, M.A., Bryant, S.L., 2013. Geometric models of porosity reduction by ductile grain compaction and cementation. AAPG Bull. 97 (12), 2129–2148. http://dx.doi.org/10.1306/05171311165.
- Needleman, A., Tvergaard, V., 1987. An analysis of ductile rupture modes at a crack tip. J. Mech. Phys. Solids 35 (2), 151–183. http://dx.doi.org/10.1016/0022-5096(87)90034-2.
- Nova, R., Castellanza, R., Tamagnini, C., 2003. A constitutive model for bonded geomaterials subject to mechanical and/or chemical degradation. Int. J. Numer. Anal. Methods Geomech. 27 (9), 705–732. http://dx.doi.org/10.1002/nag.294.
- Rattez, H., Stefanou, I., Sulem, J., Veveakis, M., Poulet, T., 2018. Numerical analysis of strain localization in rocks with thermo-hydro-mechanical couplings using cosserat continuum. Rock Mech. Rock Eng. 51 (10), 3295–3311. http://dx.doi.org/10.1007/s00603-018-1529-7.
- Reddi, D., Areej, V., Keralavarma, S., 2019. Ductile failure simulations using a multi-surface coupled damage-plasticity model. Int. J. Plast. 118, 190–214. http://dx.doi.org/10.1016/j.ijplas.2019.02.007.
- Rutter, E., Glover, C., 2012. The deformation of porous sandstones are Byerlee friction and the critical state line equivalent? J. Struct. Geol. 44, 129–140. http://dx.doi.org/10.1016/j.jsg.2012.08.014.
- Samudio, M., 2017. Modelling of an Oil Well Cement Paste from Early Age to Hardened State: Hydration Kinetics and Poromechanical Behaviour (Ph.D. thesis). (2017PESC1041), Université Paris-Est, URL https://pastel.archives-ouvertes.fr/tel-01781441.

- Sarker, M., Siddiqui, S., 2009. Advances in micro-CT based evaluation of reservoir rocks. In: All Days. SPE, http://dx.doi.org/10.2118/126039-ms.
- Saxena, N., Hows, A., Hofmann, R., Alpak, F.O., Freeman, J., Hunter, S., Appel, M., 2018. Imaging and computational considerations for image computed permeability: Operating envelope of digital rock physics. Adv. Water Resour. 116, 127–144. http://dx.doi.org/10.1016/j.advwatres.2018.04.001.
- Saxena, N., Mavko, G., 2016. Estimating elastic moduli of rocks from thin sections: Digital rock study of 3D properties from 2D images. Comput. Geosci. 88, 9–21. http://dx.doi.org/10.1016/j.cageo.2015.12.008.
- Shen, W., Shao, J., 2016. An incremental micro-macro model for porous geomaterials with double porosity and inclusion. Int. J. Plast. 83, 37–54. http://dx.doi.org/10.1016/j.ijplas.2016.04.002.
- Shen, W., Shao, J., Liu, Z., Oueslati, A., Saxcé, G.D., 2020. Evaluation and improvement of macroscopic yield criteria of porous media having a Drucker-Prager matrix. Int. J. Plast. 126, 102609. http://dx.doi.org/10.1016/j.ijplas.2019.09.015.
- Shen, W., Zhang, J., Shao, J., Kondo, D., 2017. Approximate macroscopic yield criteria for Drucker-Prager type solids with spheroidal voids. Int. J. Plast. 99, 221–247. http://dx.doi.org/10.1016/j.ijplas.2017.09.008.
- Talabi, O., AlSayari, S., Iglauer, S., Blunt, M.J., 2009. Pore-scale simulation of NMR response. J. Pet. Sci. Eng. 67 (3-4), 168-178. http://dx.doi.org/10.1016/j.petrol.2009.05.013.
- Tengattini, A., Das, A., Nguyen, G.D., Viggiani, G., Hall, S.A., Einav, I., 2014. A thermomechanical constitutive model for cemented granular materials with quantifiable internal variables. Part I—Theory. J. Mech. Phys. Solids 70, 281–296. http://dx.doi.org/10.1016/j.jmps.2014.05.021.
- Tvergaard, V., Needleman, A., 1984. Analysis of the cup-cone fracture in a round tensile bar. Acta Metall. 32 (1), 157–169. http://dx.doi.org/10.1016/0001-6160(84)90213-x.
- Veveakis, E., Regenauer-Lieb, K., 2015. Review of extremum postulates. Curr. Opin. Chem. Eng. 7, 40-46. http://dx.doi.org/10.1016/j.coche.2014.10.006.
- Vincent, P.-G., Suquet, P., Monerie, Y., Moulinec, H., 2014. Effective flow surface of porous materials with two populations of voids under internal pressure: I. A GTN model. Int. J. Plast. 56, 45–73. http://dx.doi.org/10.1016/j.ijplas.2013.11.013.
- Wen, J., Huang, Y., Hwang, K.C., Liu, C., Li, M., 2005. The modified Gurson model accounting for the void size effect. Int. J. Plast. 21 (2), 381–395. http://dx.doi.org/10.1016/j.ijplas.2004.01.004.
- Wong, T., David, C., Zhu, W., 1997. The transition from brittle faulting to cataclastic flow in porous sandstones: Mechanical deformation. J. Geophys. Res. Solid Earth 102 (B2), 3009–3025. http://dx.doi.org/10.1029/96jb03281.
- Wood, D., 1990. Soil Behaviour and Critical State Soil Mechanics. Cambridge University Press, Cambridge England New York, ISBN: 9781139878272.
- Worden, R.H., Burley, S.D., 2009. Sandstone diagenesis: The evolution of sand to stone. In: Book: Sandstone Diagenesis: Recent and Ancien. Blackwell Publishing Ltd., pp. 1–44. http://dx.doi.org/10.1002/9781444304459.ch.
- Yin, H., Dvorkin, J., 1994. Strength of cemented grains. Geophys. Res. Lett. 21 (10), 903-906. http://dx.doi.org/10.1029/93gl03535.
- Zhang, D., Zhang, R., Chen, S., Soll, W.E., 2000. Pore scale study of flow in porous media: Scale dependency, REV, and statistical REV. Geophys. Res. Lett. 27 (8), 1195–1198. http://dx.doi.org/10.1029/1999gl011101.